Full-potential linear-muffin-tin-orbital calculation of electron momentum densities of solids



1999 J. Phys.: Condens. Matter 11 6779

(http://iopscience.iop.org/0953-8984/11/35/314)

J. Phys.: Condens. Matter **11** (1999) 6779–6792. Printed in the UK PII: S0953-8984(99)03282-8

# Full-potential linear-muffin-tin-orbital calculation of electron momentum densities of solids

A S Kheifets†, D R Lun† and S Yu Savrasov‡

† Research School of Physical Sciences and Engineering, Australian National University, Canberra ACT 0200, Australia

‡ Max-Planck-Institut für Festköperforschung, 70569 Stuttgart, Germany

Received 7 April 1999

**Abstract.** We calculate electron momentum densities of various crystalline solids by employing the linear-muffin-tin-orbital (LMTO) method. We use three levels of approximation to the LMTO: the simplest atomic sphere approximation (ASA), the ASA with overlap correction, and the full-potential (FP) LMTO. Although the band energies calculated using the ASA and the FP-LMTO are practically the same, there is a noticeable difference in the electron momentum densities which is not cured by making a simple overlap correction to the ASA-LMTO method.

## 1. Introduction

The linear-muffin-tin-orbital (LMTO) method [1] is a very efficient and flexible tool which is widely used for first-principles computations of the electronic structure of solids. The need for such computations is overwhelming since a great number of physical properties of solids depend on the electronic structure. In addition, *ab initio* molecular dynamics simulations require a method which yields accurate total energies or forces.

Electronic structure calculations on crystalline solids are performed conveniently by dividing the crystal into non-overlapping muffin-tin (MT) spheres centred on atomic sites, and the remaining interstitial region. The electron density and the potential are almost spherically symmetric within the MT spheres and are essentially flat in the interstitial region. Therefore the electron wave function, the charge density, and the potential have a dual representation: a spherical harmonic expansion inside the MT spheres and a plane-wave expansion in the interstitial region.

The LMTO method is just one of many computational schemes derived within the framework of the density functional theory. The great practical advantage of the LMTO method is that only a minimal basis set of energy-independent orbitals (typically 9–16 per atom) is needed to obtain accurate eigenvalues (band energies). In the simplest ASA-LMTO method the MT spheres are expanded to the overlapping Wigner–Seitz (WS) spheres which occupy the whole volume of the crystal without there being an interstitial region. Inside the WS spheres, the LMTOs are represented by numerical solutions of the radial Schrödinger equation and their energy derivatives. Outside the WS spheres the LMTOs are augmented by the solutions of the Helmholtz equation at some fixed energy (usually $\kappa^2 = 0$).

This approach is generally sufficient for obtaining band energies with a typical accuracy of 0.1 eV. It is known, however, that it is the eigenfunctions of the Schrödinger equation rather than the eigenvectors which are more sensitive to the approximations involved in solving this

0953-8984/99/356779+14$30.00  

equation. Therefore, to reproduce observables which depend on the wave function itself, one has to resort to much more elaborate theoretical schemes. In particular, reproducing the charge-density distribution inside the crystal requires a more detailed knowledge of the electron wave function in the interstitial region.

The most stringent test of the theory would be direct experimental observation of the electron wave function in a crystal. This is not possible at present. However, there has been a technique developed recently which allows us to determine the magnitude of the electron wave functions in the momentum space [2, 3]. This technique, known as electron momentum spectroscopy (EMS), relies on an ionizing collision of a fast electron with a thin solid membrane and the subsequent detection of the scattered and ejected electrons in time coincidence with fully determined kinematics (a so-called (e, 2e) reaction). The cross-section of such a reaction is shown to be proportional to the magnitude of the electron wave function in the momentum space in a given energy band. This quantity determines the probability of finding an electron in the solid with the given values of energy and momentum (energy-resolved, or spectral, electron momentum density—EMD).

A related technique, known as a $(\gamma, e\gamma')$ reaction, has been also implemented, in which a hard x-ray photon is used as a probe [4]. In this case the energy-integrated EMD can be determined, which gives the probability of finding an electron in the solid with the given value of momentum across all of the bands and core levels.

The emergence of these techniques has provided a new incentive to perform accurate calculations of the electron momentum and energy distributions in solids. The ASA-LMTO method has long been used for this purpose. The spherical harmonic representation of the electron wave function inside the WS sphere makes the Fourier transformation particularly simple, and thus facilitates straightforward computation of the EMD from the LMTO eigenvalues and eigenfunctions [5–8]. Non-spherical corrections can be included in an approximate way by means of the reciprocal-lattice-vector summation [5].

There have been a number of investigations in which the LMTO method has been extended beyond the ASA with no shape approximation made for either the potential or the charge density inside the elementary cell. These full-potential (FP) generalizations of the ASA-LMTO method have been used with great success to calculate various properties of solids: the equilibrium structure [9, 10], lattice dynamics [11–16], electron–phonon interaction [17–19], magnetism [20–22], dielectric response [23], and Fermi surface topology [24], to name just a few.

The FP-LMTO method has also been used for EMD calculations for complex systems such as high-$T_C$ superconducting cuprates [25, 26]. However, the results were reported in terms of the two-dimensional angular correlation of annihilation radiation (2D-ACAR) which is proportional to the electron–positron pair density, i.e. the EMD weighted with the positron wave function within the solid. No other work is known to the authors in which an attempt has been made to use the FP-LMTO method for EMD calculations. It is not clear how the accurate treatment of the interstitial region and the inclusion of non-spherical terms of the potential would affect the calculated momentum density.

In the present paper we report on EMD calculations for simple solids: FCC aluminium and copper, diamond-structure silicon, and hexagonal graphite. All of these materials have been studied by EMS [27–30]. Also, the EMD of aluminium and that of graphite were investigated very recently by means of the $(\gamma, e\gamma')$ reaction [31,32]. In addition, a score of studies have been carried out on all of these materials in which the EMD was studied via the Compton scattering or positron annihilation. In both of these methods, however, less-specific information is obtained because the EMD is integrated over in one or two dimensions of the momentum. Nevertheless, there exists a considerable wealth of information on the EMD for the materials chosen here,

which makes them particularly suitable for the purposes of the present study.

A few different techniques have been developed for taking the non-spherical corrections into account in the framework of the LMTO method. They include Fourier transformations of the LMTOs in the interstitial region [11], one-centre spherical harmonic expansions within atomic cells [16], interpolations in terms of the Hankel functions [13], as well as direct calculations of the charge density in the tight-binding representation [33]. In two of these schemes [13,16] the treatment of open structures such as the diamond structure is complicated, and interstitial spheres are usually placed between the atomic spheres. Here we employ the FP-LMTO method, which makes use of the plane-wave Fourier representation [19]. This allows us to apply the FP-LMTO method for such materials as silicon and graphite without the need for the interstitial spheres.

We report the EMD calculations made using three different approximations to the LMTO: the simplest ASA, the ASA with correction for the overlapping atomic spheres [5], and the FP-LMTO. For aluminium and copper the band energies calculated with the ASA and FP-LMTO methods are practically the same. At the same time, there is a noticeable difference in the EMD which is not removed by making a simple overlap correction to the ASA-LMTO method. In sparsely packed diamond-structure crystals and hexagonal graphite, a number of additional empty spheres have to be introduced to apply the ASA-LMTO method. In contrast, there is no need for such spheres in the FP-LMTO method. Curiously enough, we found no difference either in band energies or in EMDs for silicon when the calculations were performed with the ASA and FP-LMTO methods. In contrast, for graphite both the band energies and the EMDs obtained with these two methods differ.

The rest of the paper is organized as follows. In section 2 we present the general electron momentum density formalism and its realization with the ASA and FP-LMTO methods. In section 3 we present concrete results for all of the materials studied, and conclude by discussing why the two methods may produce different or similar results.

## 2. Electron momentum density formalism

We write the one-electron wave function in a crystal in the tight-binding representation as the Bloch sum of the localized Wannier orbitals:

$$\Psi_{j\boldsymbol{k}}(\boldsymbol{r}) = \sum_{\boldsymbol{t}} \mathrm{e}^{\mathrm{i}\boldsymbol{k}\cdot\boldsymbol{t}} \sum_{\Lambda} a_{\Lambda}^{j\boldsymbol{k}} \Phi_{\Lambda}(\boldsymbol{r} - \boldsymbol{R} - \boldsymbol{t}). \tag{1}$$

Here $\boldsymbol{k}$ is the crystal momentum, $j$ the band index, $\boldsymbol{t}$ the translation vector, and $\boldsymbol{R}$ the basis vector. The label $\Lambda$ defines a Wannier orbital centred at a given site $\boldsymbol{R}$ and it comprises the site index $\boldsymbol{R}$ and a set of atomic-like quantum numbers which should be specified for any particular case. The expansion coefficients $a_{\Lambda}^{j\boldsymbol{k}}$ are found by solving the eigenvalue problem using the standard variational technique.

The momentum-space representation of the wave function $\Psi_{j\boldsymbol{k}}$ is given by the Bloch wave expansion:

$$\Psi_{j\boldsymbol{k}}(\boldsymbol{r}) = \sum_{\boldsymbol{G}} A_j(\boldsymbol{k} + \boldsymbol{G}) \mathrm{e}^{\mathrm{i}(\boldsymbol{k}+\boldsymbol{G})\cdot\boldsymbol{r}}. \tag{2}$$

Here, summation over the reciprocal-lattice vectors $\boldsymbol{G}$ extends the crystal momentum $\boldsymbol{k}$ beyond the first Brillouin zone (the Umklapp process). The Bloch wave amplitudes are expressed through the cell integrals:

$$A_j(\boldsymbol{k} + \boldsymbol{G}) = \Omega^{-1} \int_{\mathrm{cell}} \mathrm{e}^{-\mathrm{i}(\boldsymbol{k}+\boldsymbol{G})\cdot\boldsymbol{r}} \Psi_{j\boldsymbol{k}}(\boldsymbol{r})\, \mathrm{d}\boldsymbol{r}. \tag{3}$$

Here it is assumed that the wave function $\Psi_{j\boldsymbol{k}}$ is normalized in the unit cell of volume $\Omega$.

Sometimes it is more advantageous to express the Bloch amplitudes (3) through the one-centre integrals of the Wannier orbitals rather than the multicentre expansion (1). To do so, we extend the Fourier integral (3) over the fundamental region of the crystal containing $N$ cells:

$$A_j(\boldsymbol{k}+\boldsymbol{G}) = (N\Omega)^{-1}\int_{\text{crystal}} \mathrm{e}^{-\mathrm{i}(\boldsymbol{k}+\boldsymbol{G})\cdot\boldsymbol{r}}\Psi_{j\boldsymbol{k}}(\boldsymbol{r})\,\mathrm{d}\boldsymbol{r}. \tag{4}$$

The lattice summation is carried out trivially by using the summation rule

$$\sum_{\boldsymbol{t}} \exp(-\mathrm{i}\boldsymbol{G}\cdot\boldsymbol{t}) = N.$$

Finally we arrive at the desired formula:

$$A_j(\boldsymbol{k}+\boldsymbol{G}) = \Omega^{-1}\sum_{\Lambda} a_{\Lambda}^{j\boldsymbol{k}}\mathrm{e}^{-\mathrm{i}(\boldsymbol{k}+\boldsymbol{G})\cdot\boldsymbol{R}}\int_0^{\infty}\mathrm{e}^{-\mathrm{i}(\boldsymbol{k}+\boldsymbol{G})\cdot\boldsymbol{r}}\Phi_{\Lambda}(\boldsymbol{r})\,\mathrm{d}\boldsymbol{r}. \tag{5}$$

Here the limits of the three-dimensional integration indicate symbolically the whole coordinate space.

The EMD in the occupied part of the band $j$ is proportional to the squared Bloch amplitudes:

$$\rho_j(\boldsymbol{q}) = \frac{\Omega^2}{(2\pi)^3}\sum_{\boldsymbol{G}} n_{j\boldsymbol{k}}|A_j(\boldsymbol{k}+\boldsymbol{G})|^2\delta_{\boldsymbol{q},\boldsymbol{k}+\boldsymbol{G}} \tag{6}$$

where $n_{j\boldsymbol{k}}$ is the occupation number. The EMD (6) is normalized to the total number of valence electrons per unit cell:

$$2\sum_j \int \mathrm{d}\boldsymbol{q}\ \rho_j(\boldsymbol{q}) = n_e. \tag{7}$$

### *2.1. FP-LMTO formalism*

In the FP-LMTO method the space is partitioned into non-overlapping MT spheres centred on atomic sites and the remaining interstitial region (IR). The localized Wannier orbitals entering equation (1) are chosen in the form of the energy-independent LMTOs. They are constructed in the following way [19]. Outside the MT sphere (in the IR) the tail of the LMTO is chosen in the form of a spherical Hankel function (a so-called envelope function). Inside the MT sphere the envelope function is augmented by a numerical solution of the radial Schrödinger equation at a given energy $E_{\nu l}$, and its energy derivative:

$$\Phi^H_{\kappa\Lambda}(\boldsymbol{r}) = \begin{cases} \mathrm{i}^l Y_L \dfrac{(\kappa S_{\boldsymbol{R}})^{l+1}}{(2l-1)!!} h_l(\kappa r) \equiv H_{\kappa\Lambda}(\boldsymbol{r}) & r > S_{\boldsymbol{R}} \\ \mathrm{i}^l Y_L\left(\phi^{\nu}_{\Lambda}(r) + \dfrac{W\{\phi^{\nu}_{\Lambda}, h_l\}}{W\{\dot\phi^{\nu}_{\Lambda}, h_l\}}\dot\phi^{\nu}_{\Lambda}(r)\right) & r < S_{\boldsymbol{R}}. \end{cases} \tag{8}$$

Here $h_l = j_l - \mathrm{i}n_l$ is a linear combination of spherical Bessel and Neumann functions. We choose $\Lambda \equiv \{\boldsymbol{R}L\}$ where $\boldsymbol{R}$ is the site index, and the orbital momentum variable $L \equiv \{lm\}$ is a combination of the angular momentum $l$ and its projection $m$. The $Y_L$ are spherical harmonics and $S_{\boldsymbol{R}}$ is the MT radius. The Wronskian $W$ is taken at $r = S_{\boldsymbol{R}}$ to ensure continuity and differentiability at the sphere boundary.

The Bloch sum (1) of the LMTO tails (8) centred at the site $\boldsymbol{R}$ (and repeated by all translations $\boldsymbol{t}$) penetrates a neighbouring sphere located at $\boldsymbol{R}'$ where it can be expanded around the origin as

$$\sum_{\boldsymbol{t}\neq 0}\mathrm{e}^{\mathrm{i}\boldsymbol{k}\cdot\boldsymbol{t}}H_{\kappa\Lambda}(\boldsymbol{r}_{\boldsymbol{R}}-\boldsymbol{t}) = -\sum_{L'} J_{\kappa\Lambda'}(\boldsymbol{r}_{\boldsymbol{R}'})\gamma_{\Lambda'}S^{\boldsymbol{k}}_{\Lambda'\Lambda} \tag{9}$$

where $\boldsymbol{r}_{\boldsymbol{R}} \equiv \boldsymbol{r} - \boldsymbol{R} > S_{\boldsymbol{R}}$ and $\boldsymbol{r}_{\boldsymbol{R}'} < S_{\boldsymbol{R}'}$. Here we use the notation $\gamma_\Lambda = [S_{\boldsymbol{R}}(2l+1)]^{-1}$. The Fourier-transformed structure matrix $S^{\boldsymbol{k}}_{\Lambda'\Lambda}$ is defined in reference [19]. Therefore the wave function (1) can be presented as

$$\Psi_{j\boldsymbol{k}}(\boldsymbol{r}) = \sum_{\kappa\Lambda} \mathrm{i}^l Y_L(\boldsymbol{r}) \left\{ a^{j\boldsymbol{k}}_\Lambda \Phi^H_{\kappa\Lambda}(r) - b^{j\boldsymbol{k}}_\Lambda \gamma_\Lambda \Phi^J_{\kappa\Lambda}(r) \right\} \tag{10}$$

where

$$b^{j\boldsymbol{k}}_\Lambda = \sum_{\Lambda'} a^{j\boldsymbol{k}}_{\Lambda'} S^{\boldsymbol{k}}_{\Lambda'\Lambda}.$$

Here we also introduced the LMTOs which augment the spherical Bessel function inside a MT sphere:

$$\Phi^J_{\kappa\Lambda}(\boldsymbol{r}) = \begin{cases} \mathrm{i}^l Y_L \dfrac{(2l+1)!!}{(\kappa S_{\boldsymbol{R}})^l} j_l(\kappa r) \equiv J_{\kappa\Lambda}(\boldsymbol{r}) & r > S_{\boldsymbol{R}} \\ \mathrm{i}^l Y_L \left( \phi^\nu_\Lambda(r) + \dfrac{W\{\phi^\nu_\Lambda, j_l\}}{W\{\dot\phi^\nu_\Lambda, j_l\}} \dot\phi^\nu_\Lambda(r) \right) & r < S_{\boldsymbol{R}}. \end{cases} \tag{11}$$

Expression (10) is correct both inside the MTs and in the IR. However, the form of the spherical harmonic expansion is only computationally efficient when calculating MT integrals. To perform integration over the IR it is more convenient to use an alternative Bloch wave representation:

$$\Psi_{j\boldsymbol{k}}(\boldsymbol{r}) = \sum_{\boldsymbol{t}} \mathrm{e}^{\mathrm{i}\boldsymbol{k}\cdot\boldsymbol{t}} \sum_\Lambda a^{j\boldsymbol{k}}_\Lambda \tilde H_{\kappa\Lambda}(\boldsymbol{r}_{\boldsymbol{R}} - \boldsymbol{t}) = \sum_{\boldsymbol{G}} A^{\mathrm{IR}}_j(\boldsymbol{k}+\boldsymbol{G}) \mathrm{e}^{\mathrm{i}(\boldsymbol{k}+\boldsymbol{G})\cdot\boldsymbol{r}} \tag{12}$$

where, according to (5),

$$A^{\mathrm{IR}}_j(\boldsymbol{k}+\boldsymbol{G}) = \Omega^{-1} \sum_\Lambda a^{j\boldsymbol{k}}_\Lambda \mathrm{e}^{-\mathrm{i}(\boldsymbol{k}+\boldsymbol{G})\cdot\boldsymbol{R}} \int_0^\infty \mathrm{e}^{-\mathrm{i}(\boldsymbol{k}+\boldsymbol{G})\cdot\boldsymbol{r}} \tilde H_{\kappa\Lambda}(\boldsymbol{r})\, \mathrm{d}\boldsymbol{r}. \tag{13}$$

We intend to use expression (12) solely in the IR. Therefore augmentation of the Hankel function inside the MTs is not essential. Here we modified the Hankel function in such a way as to remove its singularity near the origin and to facilitate the convergence of the Fourier integral. The modified Hankel function is introduced as a solution of the non-homogeneous Helmholtz equation:

$$(-\nabla^2 - \kappa^2)\tilde H_{\kappa\Lambda}(\boldsymbol{r}) = a_l \left( \frac{r}{S_{\boldsymbol{R}}} \right)^l \exp(-r^2\eta^2 + \kappa^2/\eta^2) \mathrm{i}^l Y_L(\boldsymbol{r}). \tag{14}$$

The normalization constant $a_l$ is given in reference [19]. The parameter $\eta$ is chosen in such a way that the Gaussian approaches zero when $r > S_{\boldsymbol{R}}$. So in the IR, which is the only place that it is used in, $\tilde H_{\kappa L}(\boldsymbol{r})$ is almost identical to $H_{\kappa L}(\boldsymbol{r})$. The Fourier integral of $\tilde H_{\kappa L}(\boldsymbol{r})$ is decaying exponentially and we have

$$A^{\mathrm{IR}}_j(\boldsymbol{q}) = \frac{4\pi}{\Omega} \sum_\Lambda a^{j\boldsymbol{k}}_\Lambda \mathrm{e}^{-\mathrm{i}\boldsymbol{q}\cdot\boldsymbol{R}} Y_L(\boldsymbol{q}) \frac{S^{l+1}_{\boldsymbol{R}}}{(2l-1)!!} \frac{q^l}{q^2-\kappa^2} \exp\left( \frac{\kappa^2 - q^2}{4\eta^2_{Rl}} \right). \tag{15}$$

To evaluate the Bloch amplitudes of the wave function (10) we calculate the cell integral (3) separately over the MTs and the IR, where we use equations (10) and (12), respectively. Finally we get

$$A_j(\boldsymbol{k}+\boldsymbol{G}) = A^{\mathrm{MT}}_j(\boldsymbol{k}+\boldsymbol{G}) + \sum_{\boldsymbol{G}'} A^{\mathrm{IR}}_j(\boldsymbol{k}+\boldsymbol{G}') \frac{1}{\Omega} \int_{\mathrm{IR}} \mathrm{e}^{-\mathrm{i}(\boldsymbol{G}-\boldsymbol{G}')\cdot\boldsymbol{r}}\, \mathrm{d}\boldsymbol{r}. \tag{16}$$

The MT part of the Fourier integral $A^{\mathrm{MT}}_j$ is given by the following expression:

$$A^{\mathrm{MT}}_j(\boldsymbol{q}) = \frac{4\pi}{\Omega} \sum_\Lambda \mathrm{e}^{-\mathrm{i}\boldsymbol{q}\cdot\boldsymbol{R}} Y_L(\boldsymbol{q}) \int_0^{S_R} r^2\, \mathrm{d}r\; j_l(qr) \left\{ a^{j\boldsymbol{k}}_\Lambda \phi^H_{\kappa\Lambda}(r) - b^{j\boldsymbol{k}}_\Lambda \gamma_\Lambda \phi^J_{\kappa\Lambda}(r) \right\}. \tag{17}$$

The plane-wave integration over the IR can be carried out analytically using Green's second identity:

$$\int_{\mathrm{IR}} \mathrm{e}^{-\mathrm{i}\boldsymbol{g}\cdot\boldsymbol{r}}\,\mathrm{d}\boldsymbol{r} = \left(\Omega - \sum_{\boldsymbol{R}} \frac{4\pi}{3} S_{\boldsymbol{R}}^3\right)\delta_{g,0} - (1-\delta_{g,0}) \sum_{\boldsymbol{R}} \mathrm{e}^{\mathrm{i}\boldsymbol{g}\cdot\boldsymbol{R}} j_1(gS_{\boldsymbol{R}}) \frac{4\pi S_{\boldsymbol{R}}^2}{g}. \tag{18}$$

### *2.2. ASA-LMTO formalism*

In the ASA-LMTO formalism the unit cell is substituted for with a number of overlapping Wigner–Seitz spheres. The total volume of the WS spheres equates to the volume of the unit cell, thus eliminating the IR. The ASA-LMTO formalism can be most easily derived by first considering a slightly different but closely related formalism of the Korringa–Kohn–Rostoker (KKR) method [1].

We write the orbital-momentum-decomposed MT orbitals as

$$\Phi_\Lambda(\boldsymbol{r}) = \mathrm{i}^l Y_L(\boldsymbol{r}) \begin{cases} \phi_\Lambda(E,r) + p_\Lambda (r/S_{\boldsymbol{R}})^l & r < S_{\boldsymbol{R}} \\ (S_{\boldsymbol{R}}/r)^{l+1} & r > S_{\boldsymbol{R}}. \end{cases} \tag{19}$$

The energy-dependent radial orbitals $\phi_\Lambda(E,r)$ are found by numerical solution of the radial Schrödinger equation. The numerical orbitals $\phi_\Lambda(E,r)$ are augmented inside the sphere by a renormalized spherical Bessel function $J_{\kappa\Lambda}$, equation (11), and outside the sphere by a renormalized spherical Hankel function $H_{\kappa\Lambda}$, equation (8), both functions taken at the limit $\kappa \to 0$. Thus the tail of the MT orbitals, equation (19), at $r > S_{\boldsymbol{R}}$ is the solution of the Helmholtz equation with zero kinetic energy. The potential parameters $p_\Lambda$ are chosen in such a way as to make the wave function (19) continuous and differentiable at the sphere boundary.

Similarly to expression (9), the Bloch sum of the MT tails (19) originating at the site $\boldsymbol{R}$ and repeated by translation vectors $\boldsymbol{t}$ penetrates a neighbouring sphere located at the site $\boldsymbol{R}'$ where it can be expanded around the origin:

$$\sum_{\boldsymbol{t}\neq 0} \mathrm{e}^{\mathrm{i}\boldsymbol{k}\cdot\boldsymbol{t}} \left(\frac{S_{\boldsymbol{R}}}{|\boldsymbol{r}_{\boldsymbol{R}} - \boldsymbol{t}|}\right)^{l+1} \mathrm{i}^l Y_L(\boldsymbol{r}_{\boldsymbol{R}} - \boldsymbol{t}) = -\sum_{L'} \frac{1}{l'(2l'+1)} \left(\frac{r_{\boldsymbol{R}'}}{S_{\boldsymbol{R}'}}\right)^{l'} \mathrm{i}^{l'} Y_{L'}(\boldsymbol{r}_{\boldsymbol{R}'}) S^{\boldsymbol{k}}_{\Lambda'\Lambda} \tag{20}$$

where $\boldsymbol{r}_{\boldsymbol{R}} \equiv \boldsymbol{r} - \boldsymbol{R} > S_{\boldsymbol{R}}$ and $\boldsymbol{r}_{\boldsymbol{R}'} < S_{\boldsymbol{R}'}$. Here $S^{\boldsymbol{k}}_{\Lambda'\Lambda}$ is the canonical structure constant [1]. As the numerical orbitals $\phi_\Lambda(E,r)$ already satisfy the radial Schrödinger equation, the correct one-centre expansion inside any sphere will be $\mathrm{i}^l Y_l(\boldsymbol{r})\phi_\Lambda(E,r)$ provided that the tails from all of the other spheres cancel the term $p_\Lambda(r/S_{\boldsymbol{R}})^l$. The required tail cancellation is seen to occur if a set of the so-called KKR-ASA equations is satisfied:

$$\sum_{\Lambda'} \left[p_\Lambda \delta_{\Lambda\Lambda'} - S^{\boldsymbol{k}}_{\Lambda\Lambda'}\right] a^{j\boldsymbol{k}}_{\Lambda'\Lambda} = 0. \tag{21}$$

This leaves the Bloch sum of LMTOs inside any sphere simply as

$$\Psi_{j\boldsymbol{k}}(\boldsymbol{r}) = \sum_L a^{j\boldsymbol{k}}_\Lambda \mathrm{i}^l Y_L(\boldsymbol{r})\phi_\Lambda(E_{j\boldsymbol{k}}, r) \qquad r < S_{\boldsymbol{R}}. \tag{22}$$

The eigenvectors $a^{j\boldsymbol{k}}_\Lambda$ and eigenvalues $E_{j\boldsymbol{k}}$ should be found by solving the set of KKR equations (22). Finally we evaluate the MT integrals and obtain the Bloch amplitudes:

$$A^{\mathrm{MT}}_j(\boldsymbol{q}) = \frac{4\pi}{\Omega} \sum_\Lambda a^{j\boldsymbol{k}}_\Lambda \mathrm{e}^{-\mathrm{i}\boldsymbol{q}\cdot\boldsymbol{R}} Y_L(\boldsymbol{q}) \int_0^{S_R} r^2\,\mathrm{d}r\; j_l(qr)\phi_\Lambda(E_{j\boldsymbol{k}}, r) \tag{23}$$

where $j_l(qr)$ is the spherical Bessel function.

As the overlapping WS spheres take up the whole volume of the unit cell, expression (22) represents the electron wave function everywhere inside the cell. This allows one to calculate

the cell integral (3) without approximating it as a number of the WS sphere integrals [5]. Equation (16) now can be written as

$$A_j(\boldsymbol{k}+\boldsymbol{G}) = A_j^{\mathrm{MT}}(\boldsymbol{k}+\boldsymbol{G}) + \sum_{\boldsymbol{G}'} A_j(\boldsymbol{k}+\boldsymbol{G}')\Omega^{-1}\int_{\mathrm{cell}-\sum_{\boldsymbol{R}}\mathrm{WS}} \mathrm{e}^{-\mathrm{i}(\boldsymbol{G}-\boldsymbol{G}')\cdot\boldsymbol{r}}\,\mathrm{d}\boldsymbol{r} \tag{24}$$

where the plane-wave integral is given by (18). The first term on the right-hand side of (18) disappears, since $\Omega = \sum_{\boldsymbol{R}}\Omega_{\boldsymbol{R}}$. Finally, equation (24) can be presented as

$$A_j(\boldsymbol{k}+\boldsymbol{G}) = \sum_{\boldsymbol{G}'} A_j^{\mathrm{MT}}(\boldsymbol{k}+\boldsymbol{G}')\mathbf{M}^{-1}_{\boldsymbol{G}'\boldsymbol{G}}. \tag{25}$$

Here (25) contains the inverse of the matrix $\mathbf{M}_{\boldsymbol{G}'\boldsymbol{G}}$ which is defined as

$$\mathbf{M}_{\boldsymbol{G}'\boldsymbol{G}} = \sum_{\boldsymbol{R}} \frac{3j_1(|\boldsymbol{G}-\boldsymbol{G}'|S_{\boldsymbol{R}})}{|\boldsymbol{G}-\boldsymbol{G}'|S_{\boldsymbol{R}}} \qquad \mathbf{M}_{\boldsymbol{G}\boldsymbol{G}} = \mathbf{1}. \tag{26}$$

Thus far, we have assumed that the coefficients $a^{j\boldsymbol{k}}_{\Lambda'\Lambda}$ entering the expression for the Bloch amplitudes (22) are found by solving the KKR-ASA equations (21). However, computationally it is much more advantageous to cast these equations in the form of the Rayleigh–Ritz variational principle in conjunction with energy-independent MT orbitals. This can be done if, instead of treating the full energy dependence of the numerical orbitals $\phi_\Lambda(E,r)$ in (19), we use a Taylor expansion:

$$\phi_\Lambda(E,r) = \phi^\nu_\Lambda(r) + \dot{\phi}^\nu_\Lambda(r)(E-E_{\nu l}) + \frac{1}{2}\ddot{\phi}^\nu_\Lambda(r)(E-E_{\nu l})^2 \tag{27}$$

where $\phi^\nu_\Lambda(r)$ is the solution of the radial Schrödinger equation at a given energy $E_{\nu l}$ and $\dot{\phi}^\nu_\Lambda(r)$, and $\ddot{\phi}^\nu_\Lambda(r)$ are its energy derivatives. This definition turns the energy-dependent MT orbitals (19) into energy-independent LMTOs. The expansion coefficients $a^{j\boldsymbol{k}}_\Lambda$ are now found by solving the LMTO-ASA eigenvalue problem using the standard variational technique.

## 3. Results and discussion

The results of our calculations are presented in figures 1–4 for aluminium, copper, silicon, and graphite, respectively. In each figure we show the band energies (top row of panels) and EMDs (bottom row of panels) along several high-symmetry lines of the corresponding crystalline structure. The EMD was calculated using three different expressions for the Bloch amplitudes: equation (23) for the ASA-LMTO, equation (25) for the overlap-corrected ASA-LMTO, and equation (16) for the FP-LMTO. Although the EMDs (6) were calculated for each band individually, for the sake of clarity we present here only the total EMD

$$\rho(q) = \sum_j \rho_j(q)$$

summed over all occupied bands. In all of the calculations, the exchange and correlation part of the electron potential was calculated using the local density approximation (LDA) with the Janak–Moruzzi–Williams parametrization. We found, however, that using any particular form of the LDA parametrization has very little effect on the resulting electronic structure. Generalized gradient corrections have been attempted but showed no effect on either the band energies or the electron momentum densities.

### *3.1. Aluminium*

Aluminium is a simple nearly free-electron solid. The occupied bands disperse along a free-electron parabola with a flat momentum density interrupted by the Fermi break. The anisotropy in aluminium is very weak and can only be seen near the Brillouin zone boundaries. So this simple solid is an ideal test case for investigating the accuracy of electronic structure calculations with various levels of approximation to the LMTO method.

The band energies of aluminium calculated with the ASA and FP-LMTO methods are almost indistinguishable, as is seen from figure 1 (top panels). The slight difference can only be seen above the Fermi level. We believe that the FP band energies are more accurate, since the calculation was performed with an enlarged basis containing three different sets of orbitals with different kinetic energies $\kappa^2$ optimized for various parts of the valence and conduction bands. In the ASA-LMTO method, $\kappa^2$ is fixed to zero. In any case, the difference in electronic structure of the conduction band is largely irrelevant for the purposes of the present study, since we are concerned with occupied valence bands only.

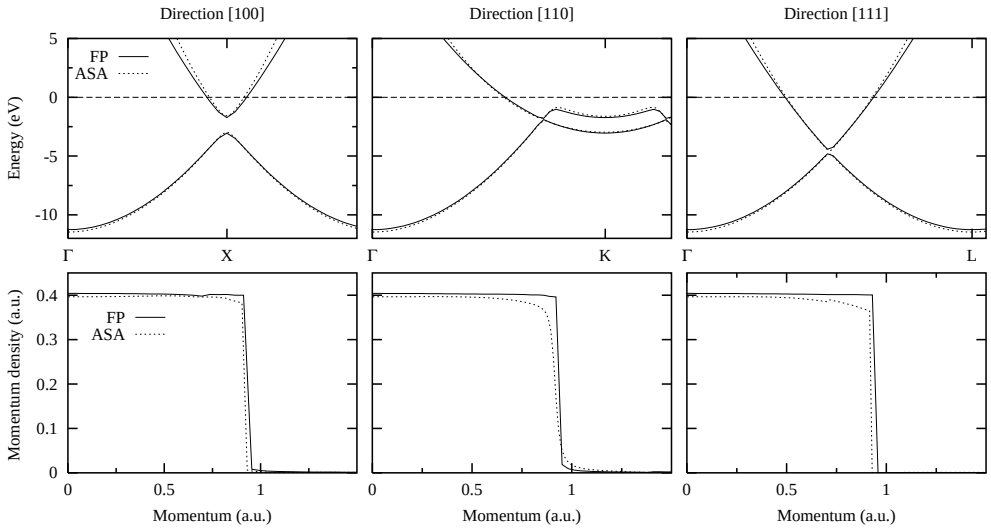


**Figure 1.** Energy bands (top row of panels) and electron momentum densities (bottom row of panels) of aluminium along several high-symmetry directions. The band energies are with respect to $E_F$. Solid and dotted curves denote the results from ASA and FP-LMTO calculations, respectively.

Although the energies of the occupied bands are practically the same in the ASA and FP-LMTO cases, the EMDs are different along all of the directions shown in the figure. The FP results tend to be closer to the step-like momentum density expected for a free-electron solid. Similar step-like behaviour was also reported by Papanikolaou *et al* [34], who employed the linear augmented plane-wave (LAPW) method in their calculations. Unfortunately, Papanikolaou *et al* [34] have not made their EMD data available in numerical form, which makes it difficult to perform a more thorough comparison.

The overlap correction to the ASA according to equation (25) does not appreciably change the EMD in any direction, and for this reason is not shown in the figure. As was pointed out in reference [5], this correction is only significant away from the first Brillouin zone where the EMD in aluminium is vanishing because of the Fermi break.

Although the improvement of the FP-LMTO EMD over the ASA one is not large in

numerical terms, conceptually it is still very important. Aluminium has been the subject of a number of investigations studying the effect of many-electron correlations on the electronic structure (the most recent is reference [31]). As the many-body effects are weak in aluminium, the one-electron calculation is required to be very accurate to leave adequate scope for many-body corrections.

### *3.2. Copper*

The electronic structure of copper is conventionally interpreted as the result of hybridization of a free-electron-like s band and atomic-like and weakly dispersive d bands. The EMD of copper at small momenta $q$ is dominated by the lowest free-electron band formed primarily from the atomic 4s states. As this band disperses upwards it crosses weakly dispersive bands originating from the atomic 3d states and acquires a considerable degree of d character. The band which intersects the Fermi level can be viewed as a continuation of the lowest s band, as it has almost no d character at the moment of intersection. The Fermi break is clearly visible in the ΓX and ΓK directions while the EMD in the ΓL direction is smooth. At larger momentum values the main contribution to the EMD comes from the atomic-like d bands and it shows a long tail extending across several Brillouin zones.

The band energies of copper calculated with the ASA and FP-LMTO methods and shown in figure 2 are generally very close except for a small deviation in the conduction band far above the Fermi level. A possible reason for this deviation was suggested in a previous section. The momentum densities are visibly different in the ASA and FP-LMTO cases. The deviation occurs near the Fermi break where a primarily s-character band crosses the Fermi level. Again, as for aluminium, the FP-LMTO form tends to produce more step-like momentum density in contrast to the ASA-LMTO form which shows some unnatural sudden increases near the Fermi break. The deviation between the ASA and FP-LMTO cases is less prominent in the ΓL direction, where the momentum density decays in an atomic-like manner.

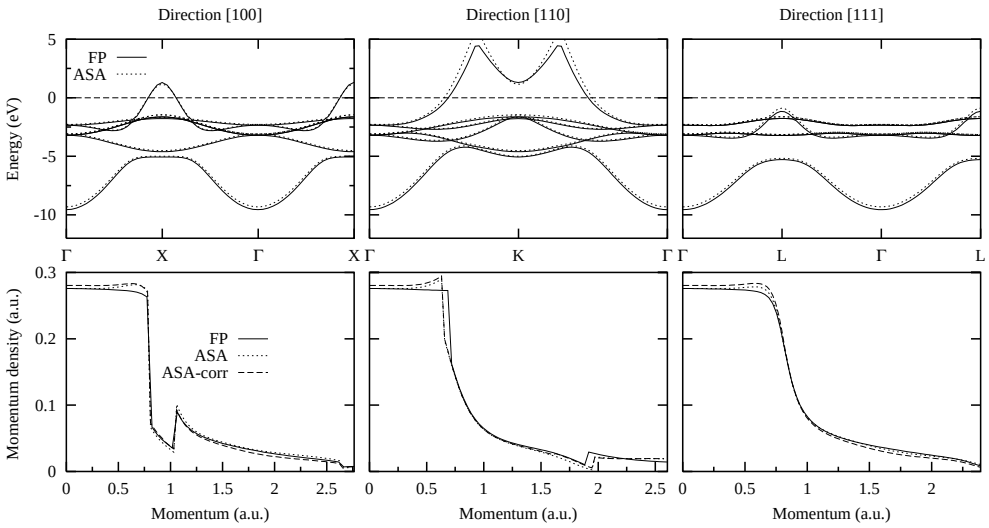


**Figure 2.** Energy bands and electron momentum densities in copper. Solid and dotted curves denote the results from ASA and FP-LMTO calculations, respectively. Dashed curves in the bottom row of panels show the ASA-LMTO calculation corrected for overlapping WS spheres according to reference [5].

This might indicate some inadequacy of the ASA-LMTO method in dealing with a free-electron-like momentum distribution at large values of $q$. As was mentioned above, the ASA-LMTO form is equipped with only one tail energy, $\kappa^2 = 0$, which might be insufficient for reproducing the plane-wave behaviour for larger $q$.

The overlap correction to the ASA-LMTO form according to reference [5] was taken into account and is shown in figure 2. Surprisingly, this caused very little change in the EMD, even away from the first Brillouin zone. The greatest mismatch between the ASA and FP-LMTO cases, close to the Fermi break, is not removed by the overlap correction.

### *3.3. Silicon*

Silicon, like any diamond-structure crystal, is a very loosely packed solid with only 0.34 of the cell volume filled with touching spheres. It has long been recognized [35] that in order to treat this crystal in the ASA-LMTO method a number of fictitious 'empty' spheres should be introduced at the interstitial sites. Conventionally, these sites are chosen to be at the high-symmetry points $(-a/4, -a/4, -a/4)$ and $(a/2, 0, 0)$, whereas the two inequivalent atomic positions are at $(0, 0, 0)$ and $(a/4, a/4, a/4)$. Here $a$ is the lattice parameter. The FP-LMTO method treats the interstitial region explicitly and does not require extra empty spheres.

The results of the ASA and FP-LMTO calculations for silicon are shown in figure 3. Unlike the cases for aluminium and copper, both the band energies and momentum densities are practically indistinguishable in the two calculations. This could possibly be explained by the fact that silicon is a dielectric and none of the occupied bands crosses or approaches the Fermi level where the main divergence of the ASA and FP-LMTO results occurs for metals. Implementing the overlap correction to the ASA-LMTO method according to reference [5] was too computationally expensive for silicon. Because of the excellent agreement between the ASA and FP-LMTO results, we do not expect this to be significant.

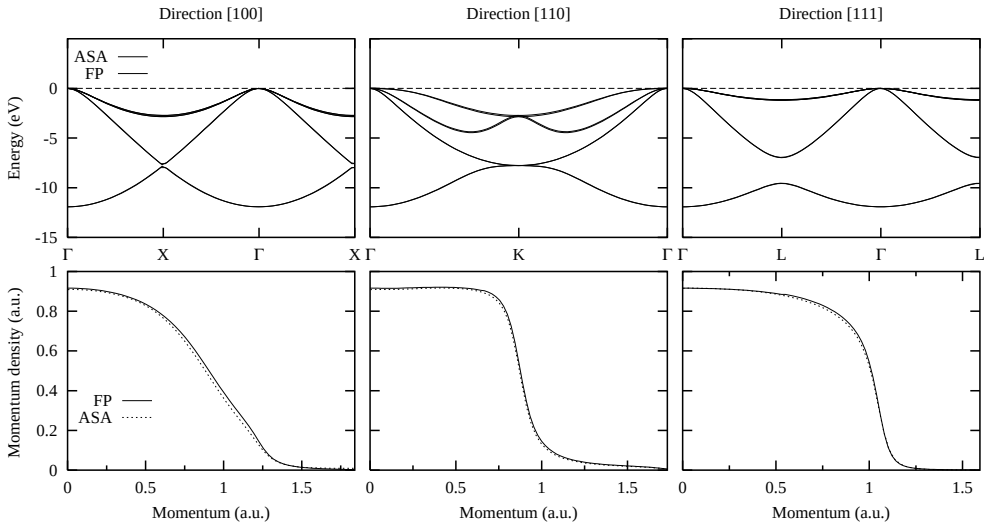


**Figure 3.** Energy bands and electron momentum densities in silicon. Solid and dotted curves denote the results from ASA and FP-LMTO calculations, respectively. Band energies are shown with respect to the bottom of the valence band.

### *3.4. Graphite*

Hexagonal graphite is an even more loosely packed solid as compared to silicon and other diamond-structure crystals. The carbon atoms in the basal plane are bound together by strong covalent bonds and form two-dimensional sheets which are held together at large distances by weak van der Waals forces. Because of the quasi-two-dimensional crystalline structure, the electron states in graphite can be classified as $\sigma$ and $\pi$ according to their reflection symmetries.

The ASA-LMTO calculation for graphite is tedious and requires a large number of empty spheres to continuously span the unit cell, which is stretched abnormally along the hexagonal axis. There is no clear recipe for finding an exact number, location or size for the empty spheres. A number of different ASA-LMTO calculations have been reported, with two [8], four [36], and eventually fourteen [37] empty spheres. The results were different, with no obvious indication of the accuracy of the calculation. The present ASA calculation was performed with four empty spheres placed at the same positions as the carbon atoms but displaced along the hexagonal axis by a quarter of the unit cell.

As was demonstrated in reference [23], the FP-LMTO method allows us to perform an accurate electronic structure calculation on graphite with no need for empty spheres at all. Not surprisingly, both the band energies and momentum densities of graphite are quite different in the ASA and FP-LMTO cases (see figure 4). Numerical values of selected band energies are presented in table 1 together with earlier FP-LMTO results from reference [23]. For comparison, we also show the results of the non-local pseudopotential calculation of Charlier *et al* [38] which is considered one of the most reliable to date. Our FP-LMTO results are very close to those of reference [23] obtained with a minimal basis set. As compared to the ASA, the FP-LMTO method improves the band energies and makes them more in line with those of Charlier *et al* [38].

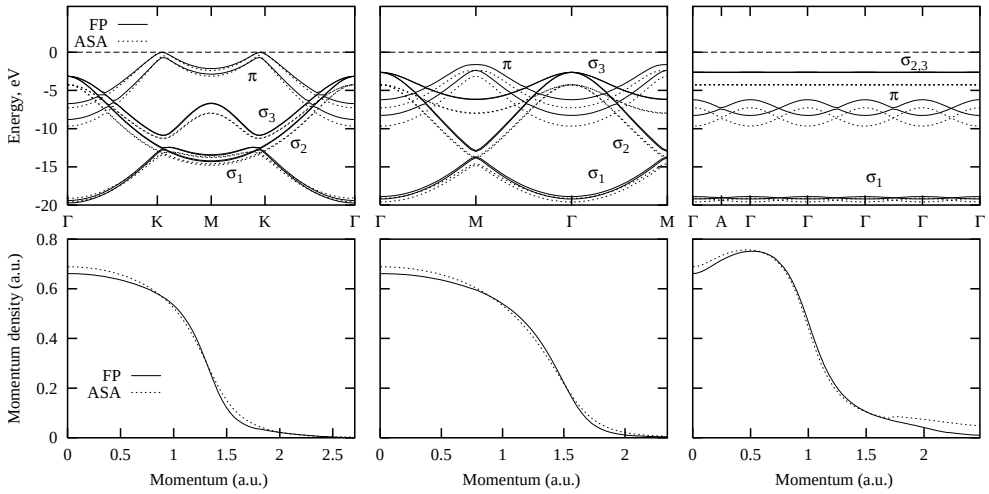


**Figure 4.** Energy bands and electron momentum densities in graphite. The key is as for figure 1.

The momentum densities derived by the ASA and FP-LMTO methods are also different. In the basal-plane directions ΓK and ΓM, the main difference is seen at small $q$-values near the Γ point. Here the main contribution to the momentum density comes from the free-electron-like lowest $\sigma_1$-band which has predominantly s character. Band energies near the Γ point are also different in the ASA and FP-LMTO methods. From this, we may conclude that the

**Table 1.** Band energies of graphite (in eV) relative to the top of the $\pi$-band.

| | | FP-LMTO | | |
|---|---|---|---|---|
| | ASA-LMTO | Present | Ahuja *et al* [23] | Charlier *et al* [38] |
| Bottom $\sigma$ | −19.59 | −19.73 | −19.55 | −20.1 |
| | −19.12 | −19.41 | −19.34 | −19.8 |
| K-point $\sigma$ | −13.42 | −12.72 | | −13.0 |
| | −11.27 | −10.87 | | −10.9 |
| Bottom $\pi$ | −9.67 | −8.79 | −8.69 | −8.9 |
| | −7.26 | −6.72 | −6.66 | −6.8 |
| Top $\sigma$ | −4.26 | −3.15 | −3.21 | −3.5 |
| Unoccupied $\sigma$ | 3.10 | 4.55 | 4.39 | 3.7 |

ASA-LMTO method does not provide an accurate description of the in-plane bonding of the carbon atoms, notwithstanding the fact that these atoms are relatively closely packed and no empty spheres are placed inside the carbon layers.

Along the ΓA direction a contribution to the EMD arises from the $\pi$-band as well. This band has predominantly p character and extends further away towards larger $q$-values where the major difference between the ASA and FP-LMTO results is seen. As the $\pi$-electrons are responsible for the interplanar bonding, this difference can be attributed to a poor description of the electron distribution between the planes where the empty spheres are inserted in the ASA.

## 4. Conclusions

In this paper we derived the electron momentum density within the LMTO method in three different approximations:

(a) The crudest ASA-LMTO approximation in which there is no room left for the interstitial area and the cell Fourier integral is substituted for with a number of integrals over overlapping WS spheres.
(b) The same as (i) but with an attempt to integrate over the interstitial region and to estimate the correction for the overlapping WS spheres.
(c) The most accurate FP-LMTO approximation in which the wave function in the interstitial region is explicitly represented by the envelope function and an exact integration over the interstitial region is performed.

We implemented this scheme to calculate the band energies and electron momentum densities in four simple solids: FCC aluminium and copper, diamond-structure silicon, and hexagonal graphite. We found that, except for graphite in which the intraplane bonding is difficult to represent even with a large number of fictitious 'empty' spheres, the band energies derived from the ASA and FP-LMTO methods are practically identical. In contrast, the electron momentum densities derived from these two methods differ noticeably. Most surprisingly, this difference is present in the simplest case of nearly free-electron-like aluminium. It is largest near the Fermi break where a flat momentum density distribution, which one would expect for a free-electron gas, is distorted in the ASA-LMTO method. The same phenomenon is observed

for copper, where the Fermi breaks in the momentum density are formed by the intersection of a free-electron-like s band with the Fermi surface. Applying a simple overlap correction to the ASA-LMTO cannot cure this anomaly for either metal.

In contrast, the FP-LMTO calculations produce reasonable EMDs which are in agreement with the literature values. We explain this phenomenon on the basis of the inability of the ASA-LMTO method to deal with free-electron-like motion of electrons with large momentum $q$ since the kinetic energy of the tails of the LMTOs is fixed at zero.

For silicon, the ASA and FP-LMTO methods agree very well, because the electrons with large momentum $q$ are significantly distorted by the lattice potential and are quite different from plane waves. The same is true for graphite. However, its abnormally loose interplanar bonding becomes a major obstacle to reproducing the electronic structure by inserting a large number of fictitious 'empty' spheres. This is why the results of the ASA and FP-LMTO calculations show large differences both in band energies and momentum densities.

In general, we suggest that the FP-LMTO method rather than the ASA-LMTO method should be used for accurate EMD calculations because of the greater care taken as regards the electron distribution in the interstitial region between the MT spheres.

## Acknowledgment

One of the authors (DRL) wishes to acknowledge support from the Australian Research Council.

## References

[1] Skriver H L 1984 *The LMTO Method (Springer Series in Solid-State Sciences vol 41)* (Berlin: Springer)
[2] Vos M and McCarthy I 1995 *Rev. Mod. Phys.* **67** 713
[3] Dennison J R and Ritter A L 1996 *J. Electron Spectrosc. Relat. Phenom.* **77** 99
[4] Bell F, Tschentscher T, Schneider J R and Rollason A J 1991 *J. Phys. B: At. Mol. Phys.* **24** L533
[5] Singh A K and Jarlborg T 1978 *J. Phys. F: Met. Phys.* **15** 727
[6] Manuel A A, Oberli L, Singh A K, Jarlborg T, Peter M, Mijnarends P E, Rabou L P L M, Hyodo T and Stewart A T 1993 *J. Phys.: Condens. Matter* **5** 8703
[7] Kheifets A S and Cai Y Q 1995 *J. Phys.: Condens. Matter* **7** 1821
[8] Kheifets A S and Vos M 1995 *J. Phys.: Condens. Matter* **7** 3895
[9] Burton B P, Osburn J E and Pasturel A 1992 *Phys. Rev.* B **45** 7677
[10] Fiorentini V, Methfessel M and Scheffler M 1993 *Phys. Rev.* B **47** 13 353
[11] Weyrich K H 1987 *Phys. Rev.* B **37** 10 269
[12] Weyrich K H, Brey L and Christensen N E 1988 *Phys. Rev.* B **38** 1392
[13] Methfessel M 1988 *Phys. Rev.* B **38** 1537
[14] Methfessel M, Rodriguez C O and Andersen O K 1989 *Phys. Rev.* B **40** 2009
[15] Rodriguez C O, Casali R A, Peltzer E L, Capannini O M and Methfessel M 1989 *Phys. Rev.* B **40** 3975
[16] Savrasov S Y and Savrasov D Y 1992 *Phys. Rev.* B **46** 12 181
[17] Savrasov S Y 1992 *Phys. Rev. Lett.* **69** 2819
[18] Savrasov S Y, Savrasov D Y and Andersen O K 1994 *Phys. Rev. Lett.* **72** 372
[19] Savrasov S Y 1996 *Phys. Rev.* B **54** 16 470
[20] Hummler K and Fähnle M 1996 *Phys. Rev.* B **53** 3272
[21] Hummler K and Fähnle M 1996 *Phys. Rev.* B **53** 3290
[22] Uebele P, Hummler K and Fähnle M 1996 *Phys. Rev.* B **53** 3296
[23] Ahuja R, Auluck S, Wills J M, Alouani M, Johansson B and Eriksson O 1997 *Phys. Rev.* B **55** 4999
[24] Ahuja R, Auluck S, Wills J M, Eriksson O, Söderlind P and Johansson B 1994 *Phys. Rev.* B **50** 18 003
[25] Barbiellini B *et al* 1991 *Phys. Rev.* B **43** 7810
[26] Blandin P *et al* 1992 *Phys. Rev.* B **4** 390
[27] Vos M, Fang Z, Canney S, Kheifets A S, McCarthy I E and Weigold E 1997 *Phys. Rev.* B **56** 963
[28] Vos M, Storer P, Cai Y Q, Kheifets A S, McCarthy I E and Weigold E 1995 *J. Phys.: Condens. Matter* **7** 279

[29] Canney S, Kheifets A S, Vos M and Weigold E 1998 *J. Electron Spectrosc. Relat. Phenom.* **88–91** 247
[30] Guo X, Fang Z, Kheifets A S, Canney S, Vos M, McCarthy I E and Weigold E 1998 *Phys. Rev.* B **57** 6333
[31] Metz C *et al* 1999 *Phys. Rev.* B **59** 10 512
[32] Metz C *et al* 1999 *J. Phys.: Condens. Matter* **11** 3933
[33] Blochl P 1989 *PhD Thesis* Max-Planck Institut für Festkörperforschung
[34] Papanikolaou N I, Bacalis N C and Papaconstantopoulos D A 1991 *Handbook of Calculated Electron Momentum Distributions, Compton Profiles and X-ray Form Factors of Elemental Solids* (Boca Raton, FL: Chemical Rubber Company Press)
[35] Glötzel D, Segall R and Andersen O K 1980 *Solid State Commun.* **36** 403
[36] Kheifets A S, Lacobucci S, Ruocco A, Camilloni R and Stefani G 1998 *Phys. Rev.* B **57** 7360
[37] Solanki A K, Kashyap A, Nautiyal T, Auluck S and Khan M A 1996 *Solid State Commun.* **100** 645
[38] Charlier J C, Gonze X and Michenaud J P 1991 *Phys. Rev.* B **43** 4579